Journal of Energy Storage 26 (2019) 101039

Contents lists available at ScienceDirect

Journal of Energy Storage

journal homepage: www.elsevier.com/locate/est

Experimental study of the impedance behavior of 18650 lithium-ion battery cells under deforming mechanical abuse

Markus Spielbauer[*,a,b], Philipp Berg[b], Michael Ringat[a,c], Oliver Bohlen[a], Andreas Jossen[b]

[a] Department of Electrical Engineering and Information Technology, Munich University of Applied Sciences, Lothstr. 64, Munich 80335, Germany
[b] Institute for Electrical Energy Storage Technology, Technical University of Munich, Arcisstr. 21, Munich 80333, Germany
[c] TÜV SÜD Battery Testing GmbH, Daimlerstr. 15, Garching 85748, Germany

ARTICLE INFO

Keywords:
18650 Lithium-ion battery
Mechanical abuse test
Deformation
Internal short circuit
Electrochemical impedance spectroscopy
Damage detection

ABSTRACT

Due to rising safety requirements for lithium-ion batteries, the detection of mechanical failure of such batteries is becoming increasingly important. As publications investigating electrochemical impedance spectroscopy (EIS) of lithium-ion battery cells under deforming mechanical abuse as a potential damage detection method are sparse, this work presents tests with stepwise loading of 18,650 lithium-ion battery cells with various impactors (nails, cylindric, hemispheric) and simultaneous EIS measurements to search for indicators which could be used to anticipate hazardous events. The occurrence of different damage mechanisms of the jelly roll is evaluated via computed tomography (μ-CT) and correlated to the measured changes in EIS.

For internal short circuits (ISCs) without instantaneous thermal runaway, the results show a decrease of ohmic resistance in the EIS for high measurement frequencies, which is possibly linked to temperature increase, while low frequencies indicate deviations from stationarity or linearity requirements. In the case of large area compression, the EIS measurements display an increase of ohmic resistance, which may be connected to various mechanisms, such as the decrease of porosity of the separator and the active materials or delamination.

1. Introduction

In recent years, the demand for lithium-ion batteries has shown expedited growth with further increases expected in the upcoming years. In a wide range of applications from the automotive sector to smartphones and power tools, the cells undergo various types and intensities of mechanical loads such as vibration, shocks or even deforming events. Although cell manufacturers put significant effort in safe and robust cell design for lithium-ion batteries to withstand such loads as well as in extensive safety tests according to various standards and regulations, multiple hazardous incidents have been reported [1–6]. Due to a growing number of battery systems in use and due to the rise in energy densities in upcoming cell generations, the number and severity of such incidents are likely to rise, which will further increase the importance of battery safety.

For this reason, the implementation of another safety layer within the battery management system (BMS), which uses extensive detection and diagnosis tools, becomes more and more viable for applications that are possibly endangered by mechanical deformation. Potential scenarios are, e.g., to alert users or rescue forces about an imminent hazardous event or to evaluate a load limit after crash incidents for the further or second use of batteries. For the development of such methods, advanced knowledge regarding damage mechanisms under mechanical deformation and corresponding electrical behavior is essential.

Regular abuse tests are defined in various standards and have been subject to a multitude of scientific publications. Ruiz et al. [7] offer an overview of both regional and international abuse testing norms and standards for lithium-ion batteries. These often set pass criterions as the absence of potentially dangerous events as “no fire”, “no explosion” or “no leakage”, which may be sufficient for regular safety testing, but do not promote a deeper understanding of the numerous effects due to mechanical abuse [6,7]. Apart from testing standards, a wide range of scientific publications [8] is available that focus mainly on cylindric

Abbreviations: BMS, Battery Management System; EIS, Electrochemical Impedance Spectroscopy; IC-DV, Incremental Capacity - Differential Voltage; ISC, Internal Short Circuit; CC, Constant Current; CV, Constant Voltage; pOCV, Pseudo Open-Circuit Voltage; SOC, State of Charge; SOH, State of Health; SOP, State of Power; SOS, State of Safety; Z-HIT, Zweipol-Hilbert-Transformation

* Corresponding author at: Department of Electrical Engineering and Information Technology, Munich University of Applied Sciences, Lothstr. 64, 80335 Munich, Germany.
E-mail address: markus.spielbauer@hm.edu (M. Spielbauer).

https://doi.org/10.1016/j.est.2019.101039
Received 9 August 2019; Received in revised form 25 October 2019; Accepted 25 October 2019
Available online 01 November 2019

[9–23] or pouch cells [9,17,24–32,32–34] and in which various formats, cell chemistries and states of charge (SOCs) are being investigated. In these publications, various impactors such as nail [9,10,22,35], conical [31], hemispheric [16–18,24–31,33,34], cylindric [14–21,25], three point bending [14–16,21,30], blunt [9,19–21,25,31] or flat [11–16,18–21,23,30–32,32] geometries with different dimensions are being used. Most tests are executed with transient or pseudo-static path controlled feed rates [9–11,13–21,23–32,32,34], yet some also present tests with impulse depending impact [12,19,20,32,32,33,36]. While most of these publications are tracking displacement, force, voltage and some temperature, the majority focus on the development of finite volume element models. Only few of them lay focus on the electrical behavior or possible detection methods of mechanically damaging events.

Regarding the detection of damages, for conventional aging, a wider range of publications is available that present detection methods such as incremental capacity-differential voltage (IC-DV), pseudo open-circuit voltage (pOCV) or electrochemical impedance spectroscopy (EIS) [37–39].

The EIS is applied by Love et al. [40,41] for state of health (SOH) monitoring of serial packs as single point measurements with a frequency of 316 Hz. Multiple publications use impedance spectroscopy for internal temperature monitoring [42–46], and Srinivasan et al. [47] implement the monitoring of impedance phase shifts to detect heating induced thermal runaways. Seifert and Schmidt [48] propose a method that uses EIS for structural monitoring of automotive lithium-ion battery packs but focus rather on the impact of different bracing pressures than on critical deforming loads. For the calculation of a proposed state of safety (SOS) Cabrera-Castillo et al. [49] use, among other measurands, impedance, and include deformation tests with different hemispheric impactors in the calculation of their SOS. While this is the only publication known to the authors to combine destructive mechanical abuse tests and impedance spectroscopy, it does not explicitly present experimental results of EIS measurements.

For this reason, this publication investigates the impact of deforming mechanical abuse on impedance spectroscopy to evaluate it as a potential method to detect critical safety states and imminent hazardous events after cell deformation. Impedance measurements are combined with micro-X-ray computed tomography (μ-CT) to correlate mechanical damage mechanisms and the impact on EIS. Based on the observations, an assessment is made regarding the implementability of EIS as a damage detection method for mechanical deformation.

2. Experimental

The basic idea of the experiments presented in this publication is to measure the impedance during a quasi-static deformation or perforation of a battery cell. These experiments aim to generate a better understanding of the effects of various damage mechanisms on the impedance behavior of the cell and to analyze if there are early indicators in the EIS that could be suitable for the detection of cell deformation. For this reason, a test setup with stepwise mechanical loading was developed, which is being presented in this section.

2.1. Testing system and feeding unit

The tests were performed at TÜV SÜD Battery Testing GmbH within a safety testing chamber. The chamber features reinforced concrete walls, explosion-proof windows, a fire suppression system and an exhaust gas purifying system to ensure safety for operators and the environment. All components of the testing and measurement system were triggered by a control PC.

An electric linear cylinder CMS71L/BS/TF/AS1H/SB1 was used as the press, which can apply maximum loads up to 20 kN, but was limited by the control software to 15 kN. As a compromise between test speed and stationarity, the tests in this study were performed with stepwise path controlled feed of 0.2 mm per step at the minimum feed rate of 0.1 mm s^{-1} for this press. The impactor was kept at a fixed position for 90 s between each feed step. This duration was chosen according to the necessary time to measure the impedance spectrum during these static phases. This stepwise feed rate was applied after bringing the impactors in contact to the cell at a constant feed rate and exceeding a certain force threshold for each impactor.

2.2. Impedance measurement

For the impedance measurements, a Gamry Interface 5000E was used in galvanostatic mode with an AC of 100 mA RMS. As different measurement frequencies might exhibit different behaviors under mechanical deformation, a frequency range from 10 kHz to 0.25 Hz was selected with ten points per decade for frequencies above 10 Hz and 5 points per decade below 10 Hz, which results in a total amount of 39 measurement points. The selected measurement option *fast* repeats up to 8 sine waves for frequencies bigger than 1000 Hz, up to 6 for frequencies bigger than 30 Hz, up to 4 for frequencies bigger than 1 Hz and up to 2 for lower frequencies or ends the measurement earlier when a specified precision criterion is fulfilled. These settings allowed the tracking of a wide range of frequencies, even reaching into the diffusive branch of the impedance spectra at a moderate measurement time of around 60 s. The impedance spectroscopy measurement was triggered 15 s after each feed step resulting in approximately 15 s of rest time at the end of each measurement until the start of the next feed step. This proceeding was continued until a thermal event occurred, the cell voltage dropped below 0.5 V or the maximum force of 15 kN was reached. To reduce fluctuations in the EIS, as they appear after a longer rest time due to long-term equalization effects [50], 20 EIS measurements were performed with each cell before the test execution to bring the cell into a more stationary state.

Due to errors in the communication between the control PC and the electric cylinder, occasional resets of the impactors position occurred, which can be observed in drops of force, as shown in the following section. Because this study focuses mainly on the impedance behavior of the cells, and as there was no significant impact on the trend in the EIS observable from these errors in communication, it was chosen to carry on with the same test settings. In case the EIS measurement had not finished before the reset, the measurement was repeated at the same indentation position.

2.3. Further measurements

A data acquisition system from Gantner Instruments was used to track the resulting force on the cell holder with a compressive force sensor K-450 supplied by Lorenz Messtechnik GmbH. Additionally, the temperatures in the testing chamber and on the cell surface were logged. Each of these measurands was recorded with a frequency of 100 Hz. The data logging for these further measurements was also continued after reaching one of the termination criteria for the feed.

2.4. Cell type and SOC

The experiments in this study were performed with the cylindric cell Samsung INR18650-25R, which has a nominal capacity of 2500 mAh and a maximum constant discharge current of 20 A. To investigate the mechanical structure of this cell type, CT scans were performed on a GE phoenix nanotom s research|edition with a voltage of ~120 kV, ~130 mA cathode current, 2x2 binning and 1000 images per scan. The CT scans, as depicted in Fig. 1, revealed that this cell type features no mandrel, one cathode tab within the jelly roll layers (green) as well as two anode tabs, which are aligned in the middle of the cell and between the jelly roll and the cell can (blue).

As the SOC has both a strong impact on the thermal runaway behavior in mechanical abuse tests [10,51] and on the electric impedance

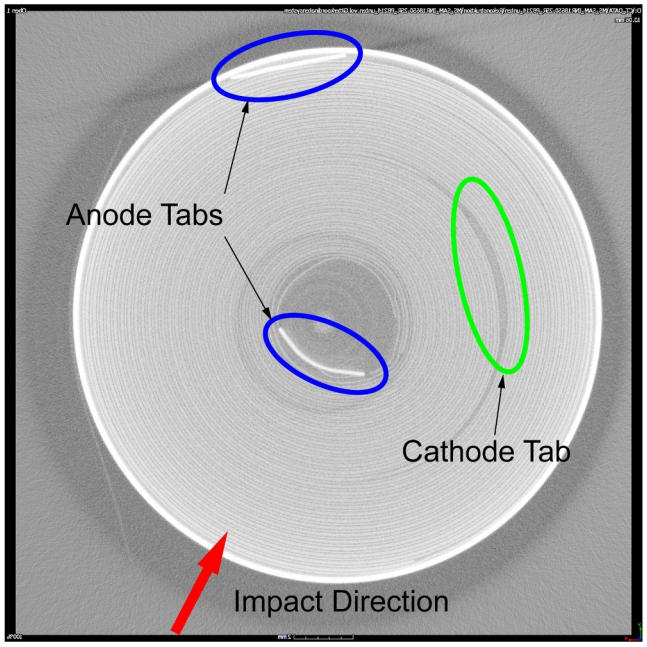

Fig. 1. Cross section of a µ-CT-Scan of the Samsung INR18650-25R cell showing the anode tabs (blue), the cathode tab (green) and the impact direction (red). . (For interpretation of the references to color in this figure legend, the reader is referred to the web version of this article.)

[40,42,44,52], different SOCs of 0%, 50% and 100% were investigated. The SOCs were applied after three checkup cycles with constant current-constant voltage (CC-CV) charge and discharge, both with 1 A and a termination criterion of 0.1 A for the CV phase. For the pre-cycling, the temperature chamber ATT Discovery DM340 was used at 25 ˚C.

2.5. Load direction and impactors

For all experiments, the cells were loaded in the radial direction with equal distance from both poles. To reduce potential tab alignment induced fluctuations in the tests, the position of the inner anode tabs of all cells were marked using CT scans. Before the test execution, the cells were aligned in the direction of the impactor, as depicted in Fig. 1. The cells were held in position by four bolts to prevent radial slippage.

Three different impactors, each of them made of steel, were chosen with the intent to provoke various failure mechanisms of the cell. For larger area squashing, a cylindrical geometry with a diameter of 20 mm was applied. For local damaging of the outer cell area, a sharpened steel nail with a diameter of 3 mm was chosen. To cause both squashing and local damaging in the same test, a hemispheric impactor with a diameter of 5 mm was selected.

2.6. Cell connection and cable alignment

To enable four-terminal sensing, which is required for high quality impedance measurements, the cells were attached with nickel-plated steel strips (HILUMIN). These were resistance spot-welded to the poles to allow the connection of the cell to the measuring equipment via screw joints of banana jacks. This facilitated a short set-up time and the establishment of a high-quality connection regarding both measurement reproducibility and mechanical stability. To reduce the electrical interference, to which the feed unit contributed, the sense and power cables were aligned orthogonally or twisted where possible. An illustration of the test setup is depicted in Fig. 2.

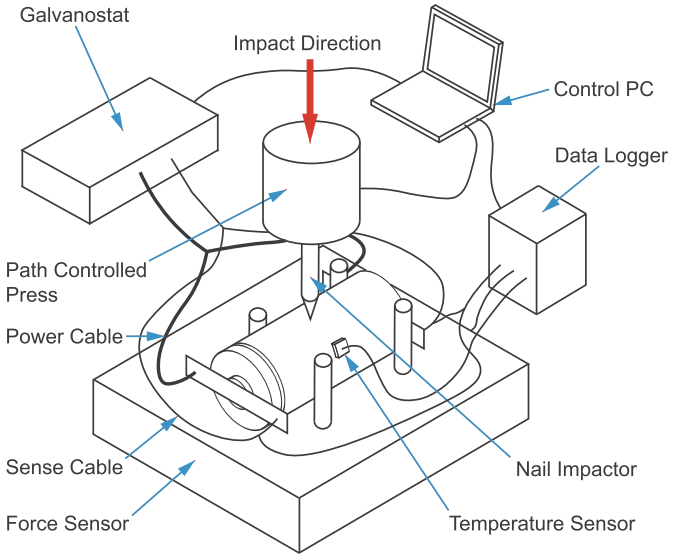

Fig. 2. Illustration of the test setup for mechanical abuse tests with impedance measurements. The PC is controlling the press, the galvanostat and the data logger. The galvanostat is four-terminal connected to the cell by screw joints mounted onto steel strips. Cables for impedance measurements are aligned orthogonally or twisted where possible. The data logger tracks signals from force and temperature sensors and is connected with the cell by the sense cables for voltage measurement.

3. Results

3.1. Measurement results

For each test, the measurement results are depicted in a figure which shows force F, cell voltage U, and cell temperature T over time t. It is remarkable that, while the impactor position is static between the feed steps, the force curves do not show static behavior but decreases in these phases, which can be attributed to slow hysteresis and relaxation effects of the cell and the test setup. The EIS measurements are displayed as a Nyquist plot in another figure with corresponding colors marked by a colorbar. In total 9 variations were conducted with one test each. To investigate the reproducibility the test with cylindric impactor and 100% SOC was carried out twice as shown in Fig. A.11. Due to test time limitations, further investigations of reproducibility could not be conducted. An overview of the conducted tests, with the corresponding test end criterions, the intrusion at first ISC and the maximum intrusion as well as the changes in ohmic resistance before the occurrence of the first ISC ΔR_i, is presented in Table 1.

3.1.1. Abuse tests with a nail impactor

For the nail penetration test in Fig. 3a with a 100% SOC, the impedance spectra depicted in Fig. 3b show no significant changes until EIS 9. After this corresponding feed step, the nail penetrates the battery case and outer jelly roll layers, which instantaneously causes a thermal runaway with a maximum temperature of 550 ˚C measured by the sensor on the cell can surface. The last measurement, EIS 10, during thermal runaway, shows a significant shift in the Nyquist plot to the left for high frequencies and almost pure ohmic behavior for frequencies below 100 Hz.

For the nail penetration test with SOC 50% (Fig. 3c), in EIS 11 the first rise in temperature and drop in voltage is observable, which indicates a first microscopic internal short circuit (ISC). During the following feed steps, a further increase in temperature and a drop in voltage can be observed. After EIS 14 thermal runaway occurs, resulting in a maximum temperature of 430 ˚C. The corresponding impedance spectra in Fig. 3d show only slight drifts in the low-frequency region

Table 1
Overview over the conducted tests with test end criteria, intrusion at first ISC and the maximum intrusion as well as the change in ohmic resistance between the first measurement and the measurement before the first occurrence of ISC.

Test	Impactor	SOC	End Criterion	ISC Intrusion	Max. Intrusion	ΔR_i
1	Nail ⌀ 3 mm	100%	Thermal runaway	1.8 mm	1.8 mm	−0.005 mΩ
2	Nail ⌀ 3 mm	50%	Thermal runaway	2.2 mm	3.0 mm	−0.070 mΩ
3	Nail ⌀ 3 mm	0%	Low voltage	2.0 mm	3.0 mm	−0.022 mΩ
4.1	Cylindric ⌀ 20 mm	100%	Maximum force	8.6 mm	8.6 mm	0.904 mΩ
4.2	Cylindric ⌀ 20 mm	100%	Maximum force	8.4 mm	8.4 mm	1.003 mΩ
5	Cylindric ⌀ 20 mm	50%	Maximum force	8.2 mm	8.2 mm	0.753 mΩ
6	Cylindric ⌀ 20 mm	0%	Maximum force	9.2 mm	9.2 mm	0.693 mΩ
7	Hemispheric ⌀ 5 mm	100%	Thermal runaway	6.4 mm	6.4 mm	0.366 mΩ
8	Hemispheric ⌀ 5 mm	50%	Thermal runaway	6.0 mm	6.0 mm	0.195 mΩ
9	Hemispheric ⌀ 5 mm	0%	Low voltage	6.6 mm	7.2 mm	−0.076 mΩ

before the ISC. In the penetration phase, a drop of ohmic resistance with a maximum of ∼1.5 mΩ for high frequencies above 100 Hz can be observed, also with changes in inductivity, while the spectrum appears to be unstructured and shows leaps for lower frequencies. The last EIS 15 during thermal runaway shows a similar shift like the prior test.

The nail penetration test with SOC 0%, depicted in Fig. 3e, exhibits the first drop in voltage and a slight increase in temperature after EIS 10. Even though a significant drop in voltage can be observed in the following feed steps, the temperature increase stays on a moderate level with a maximum of only 36 °C due to the low energy content of the cell. Remarkable are the small disturbances in the voltage curve, which represent the voltage changes due to the EIS measurement that appear larger for low SOCs due to the steeper voltage curve in these areas. The impedance measurements in Fig. 3f show negligible changes before the cell penetration with minor decreases of ohmic resistance afterwards for higher frequencies. Lower frequencies also appear to be unstructured and show a strong increase of the radius of the corresponding half circle.

3.1.2. Abuse tests with a cylindric impactor

The abuse test with the cylindric impactor and 100% SOC in Fig. 4a depicts two drops (at 1200 s and 2900 s) in the force curve due to the miscommunications with PC and the electric cylinder mentioned in subsection 2.1. Apart from this, there are no irregularities in force, temperature or voltage until the test procedure ends when the maximum impactor force of 15 kN is reached. At this point, the impactor resets its position and a sudden drop in the load curve can be observed. The impedance in Fig. 4b shows a steady and mainly ohmic increase in resistance of ∼0.9 mΩ for high frequencies and slightly larger values for low frequencies. Very high frequencies close to 10 kHz also show increasing changes in inductivity. For the first measurements, some outliers can be observed for high frequencies, which can be attributed to electromagnetic interference. A repetition of this test (Test 4.2 in Table 1, Fig. A.11), which was performed to investigate the reproducibility, shows very similar behavior regarding impedance with an increase of ohmic resistance of ∼1.0 mΩ, but with the occurrence of a soft ISC after reaching the maximum impactor force.

For the test with 50% SOC in Fig. 4c, one communication error occurred until the maximum force was reached, which resulted in a reset of the press due to the force limitation. This unloading triggered an ISC reaction with a continuous voltage drop, yet without reaching critical temperature for a thermal runaway. The impact of the squashing on the EIS in Fig. 4d is very similar to the behavior of the 100% SOC cell, with a maximum ohmic increase of around 0.75 mΩ and inductive changes only for very high frequencies.

In the test with 0% SOC in Fig. 4e, two miscommunications occurred, but apart from this no significant changes can be reported until the impactor reached the force maximum. Similar to the previous tests with the cylindric impactor, the impedance in Fig. 4f mainly shows an increase in resistance with a maximum of ∼0.69 mΩ for high frequencies. Low frequencies demonstrate an arc-like course, which is being discussed in subsection 4.1.

3.1.3. Abuse tests with a hemispheric impactor

In the test with the hemispheric impactor and 100% SOC, as depicted in Fig. 5a, two communication errors occurred. After the second error, thermal runaway occurred, which resulted in a maximum measured temperature of 580 °C. Before this, no drop in voltage or rise in temperature could be observed that could indicate a micro ISC. The Nyquist plot for this test Fig. 5b displays in an increase in ohmic resistance, which is systematically very similar to the cylindric tests, but with smaller absolute changes of only ∼0.37 mΩ. EIS 34 after thermal runaway exhibits a shift of inductive resistance for high and ohmic behavior for low frequencies.This pattern is comparable to the behavior after exhibited thermal runaway for the nail penetration tests.

Similar behavior can be reported for the test with 50% SOC in Fig. 5c, with a maximum temperature of 265 °C on the surface of the cell and no change in temperature or voltage before the thermal runaway. The thermal runaway did not occur right after the feed step but with some delay during the static phase, where a small spike in voltage was observable. This thermal runaway happened during the recording of EIS 30, as depicted in Fig. 5d, so high frequencies were still measured properly, while lower frequencies were measured during thermal runaway and demonstrate leaps and a shift towards mainly ohmic behavior. Before that, a steady increase of ohmic resistance was observable, however with a smaller absolute increase of ∼0.20 mΩ than for the 100% SOC cell. The inductive behavior shows changes for very high frequencies only.

Fig. 5e shows the measurements for the test with 0% SOC, in which one communication error resulted in a drop of the force curve. The voltage curve shows a first small drop before the measurement of EIS 33 and a significant drop to 0.5 V before EIS 35. The temperature curve displays slight increases beginning after the first voltage drop with a maximum of 27 °C. Before the occurrence of ISC, the EIS measurements in Fig. 5f show only minor changes for high frequencies in comparison with the other compressive tests. For low frequencies, the changes before ISC are mainly inductive. After the occurrence of the first short circuit, EIS 33 exhibits a very small decrease of ohmic resistance for high frequencies and inductive changes for very high frequencies. Low frequencies show an unstructured measurement curve with leaps between the measurement points.

3.2. Analysis of CT scans after test execution

To investigate how the abuse tests influenced the inner cell structure and to correlate the changes in the impedance spectra with damage mechanisms, CT scans, as depicted in Fig. 6, were conducted after the test execution. Hereby the radial cross-sections of the CT scans are aligned in the axial position of the maximum impactor penetration. For safety reasons, all cells that did not exhibit thermal runaway were deeply discharged to 0 V before the CT scans were conducted.

Table 2
Linearized impedance gradients due to temperature change in mΩ K $^{-1}$ between 15 °C and 25 °C for various SOCs at 1000 Hz and 0.25 Hz.

SOC	1000 Hz		0.25 Hz	
	ΔZ_{Re} /ΔT in mΩ K^{-1}	ΔZ_{Im} /ΔT in mΩ K^{-1}	ΔZ_{Re} /ΔT in mΩ K^{-1}	ΔZ_{Im} /ΔT in mΩ K^{-1}
100%	−0.064	0.058	−0.794	0.054
50%	−0.054	0.049	−0.567	0.026
0%	−0.054	0.050	−2.304	1.484

3.2.1. CT scans of tests with nail impactor

For all scans of nail penetration tests, the immediate deformation zone was limited to the impact spot of the nail, where it pierced the outer electrode layers (green) without causing any deformation to the inner cell structure. Nevertheless, the scans of the tests with 50% and 100% SOC show increased structural damage due to thermal runaway, especially in the inner part of the jelly roll, which is a sign of temperature gradients during the thermal runaway [53] or may hint towards lower initial mechanical stability. According to Finegan et al. [53], the bright globules that can be found in the CT scan of the 100% SOC cell consist of melted copper from the anode current collectors. This indicates that the inner cell temperature exceeded 1085 °C, which is the melting point of copper and is significantly above the maximum measured cell surface temperature of 560 °C.

3.2.2. CT scans of tests with cylindric impactor

Unlike for the nail penetration tests, the cylindric impactor leads to significant and inhomogeneous deformation in the inner part of the cells. The CT scan of the unloaded and relaxed 0% SOC cell displays a maximum compression of the jelly roll of ∼15% after unloading, as a significant part of the deformation is also compensated by the filling of the center of the cell due to the lack of a mandrel. This effect leads to significant bending of the inner anode tab and buckling of the jelly roll layers (red), as well as barely visible delamination in these areas. Additionally, the formation of large-area cracks in the jelly roll (blue) can be observed for the 50% and 100% SOC cells. Despite the severity of the damage, the 100% SOC cell remained, in principle, technically functional. Post mortem analysis in Fig. 7 revealed, that the cracks occur mainly in the cathode and anode, while the separators show imprints of these cracks but remain intact and prevent direct contact between the electrodes and thereby thermal runaway. For the cells with 0% and 100% SOC, the test stopped before reaching a critical deformation level due to the maximum force limitation and the 50% SOC cell only showed a soft ISC with limited thermal reactions, which is why none of these cells show signs of significant structural damage due to thermal runaway.

3.2.3. CT scans of tests with hemispheric impactor

Like the cylindric impactor, the hemispheric impactor causes significant deformation of the inner parts of the cells. While the CT scan for the 0% SOC cell displays a maximum compression of the jelly roll layers of ∼20% in the direct impact area, which is even larger than for the cylindric impactor, this compression and the resulting inhomogeneity affects a significantly smaller part of the cell. Similar to the cylindric impactor abuse tests, the hemispheric tests show filling of the inner cell area, bending of the inner anode tab and buckling of the jelly roll layers. The SOC dependency on the cell structure appears to be similar to the nail penetration test with the difference that the 100% SOC cell shows even larger void areas (yellow). The reason for this is that this cell not only had a larger opening of the case at the impact position, it also exhibited an even larger crack in the area of the top of the jelly roll, where combustion gases and cell material streamed out of the cell during the thermal runaway.

4. Discussion

CT scans revealed various damaging mechanisms for the different impactor types. Based on these observations, the following section discusses which mechanisms are responsible for the changes in the EIS measurements in the case of compression and due to mild ISC and whether they represent potential approaches for damage detection.Before discussing the mechanisms, it is necessary to evaluate, which measurement results can be attributed to the mechanical deformation and which may have occurred due to environmental influences.

4.1. Sensitivity of impedance spectroscopy

Impedance measurements of lithium-ion batteries are very sensitive to both SOC and temperature. While the SOC can be held almost constant using galvanostatic mode, slight temperature deviations in the range of +/−1 K could be observed even before ISCs due to the exhaust system of the safety testing chamber. To evaluate which changes in the EIS are significant enough to be attributed to the mechanical abuse rather than temperature drifts, Table 2 shows EIS changes due to temperature variations exemplary for 1000 Hz for high frequencies and 0.25 Hz for low frequencies.

For the frequency of 1000 Hz, the changes due to observed temperature drifts with a maximum of −0.064 mΩ K^{-1} in Z_{Re} are minor when compared to the shifts after large area compression, which exhibit a minimum shift of at least 0.69 mΩ for the cylindric impactors and also for the ∼0.2 mΩ increase for the hemispheric impactor with 50% SOC.

For the frequency of 0.25 Hz, temperature changes have a significant impact on the impedance spectrum for 100% and 50% SOC cells with up to −0.794 mΩ K^{-1} in Z_{Re}. Hence, changes at very low frequencies can not unequivocally be attributed to the mechanical deformation, even though temperature drifts are to some degree compensated by the thermal mass of the cell. For the cells with 0% SOC, the influence of temperature and also of relaxation effects [50] on the EIS with −2.304 mΩ K^{-1} in Z_{Re} is so significant that even temperature drifts of only 1 K can exceed the measured impedance changes in the abuse tests. Due to these large gradients, parameter fitting was not performed for parameters depending on lower frequencies (e.g. the charge transfer resistance R_{CT}). Consequently, the presentation of the results and the discussion of pre-ISC effects both focus mainly on the impedance behavior of high frequencies, especially the R_i. Since these show also significantly less sensitivity to SOC changes [40,42,44,52], they are probably more suitable for diagnostic applications anyways.

4.2. Behavior due to ISC

In the chosen setup, the nail penetration test at 100% SOC led to instant thermal runaway without prior signs in the impedance spectra that could be attributed as a sign of the upcoming ISC and thereby allow early detection. Measurements after thermal runaway (e.g. EIS 34 in Fig. 5b) show a shift in the Nyquist plot with inductive components for very high frequencies and solely ohmic behavior for lower frequencies. This behavior indicates a metallic connection between the battery poles as a test on conductor cables showed similar patterns for impedance measurements.

In the tests without instantaneous thermal runaway, the EIS measurements showed signs of invalidity for frequencies below 100 Hz and decreasing ohmic resistance for higher frequencies. While at this point the damage is usually irreversible, there could still be the chance to alert users about the unsafe state of the battery and a potentially imminent thermal runaway, which is why this behavior is being discussed in the following paragraphs.

4.2.1. Change in ohmic resistance for higher frequencies

For ISCs that did not result in thermal runaway, decreases in ohmic

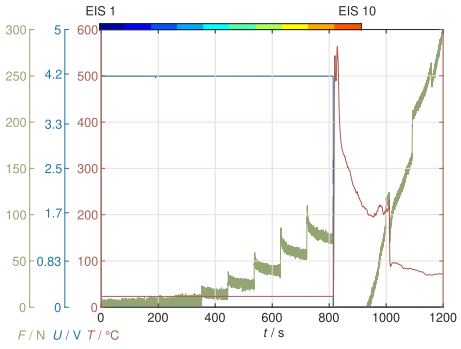

(a) F, U and T for nail impactor at 100 % SOC.

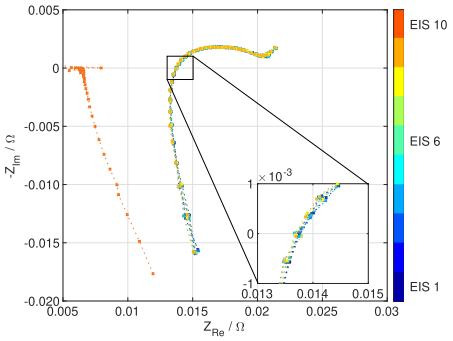

(b) Nyquist plot for nail impactor at 100 % SOC.

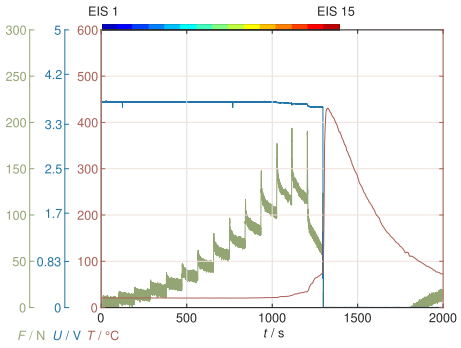

(c) F, U and T for nail impactor at 50 % SOC

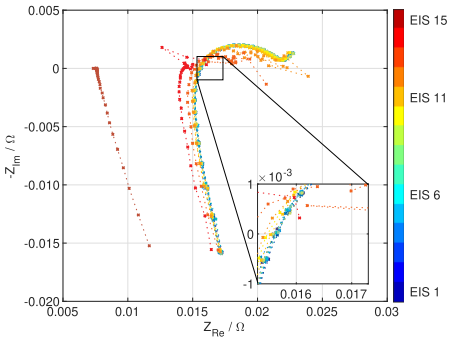

(d) Nyquist plot for nail impactor at 50 % SOC.

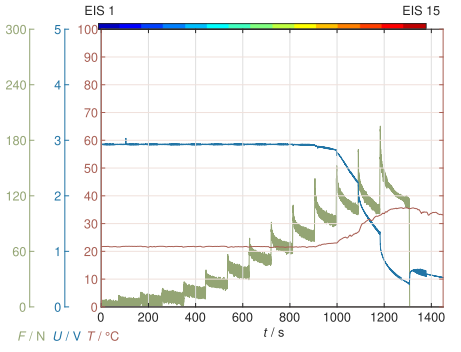

(e) F, U and T for nail impactor at 0 % SOC .

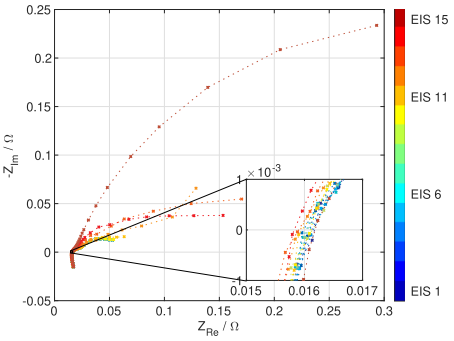

(f) Nyquist plot for nail impactor at 0 % SOC.

Fig. 3. Force, voltage, temperature (left column) and impedance measurements (right column) for abuse tests with nail impactor at various SOCs.

resistance and changes in inductivity were observed for high frequencies. This behavior might be linked to absolute change in cell temperature due to the heat released at the electrode layers in direct contact and shorting on the impactor [7]. An argument for this assumption is presented in Fig. 8 with EIS measurements at variable temperatures on the same cell type, which show similar decreasing behavior for multiple frequencies when compared with the temperatures and impedance measurements in Fig. 3d for the nail penetration test with 50% SOC. This hypothesis is also supported by the observation that there is a smaller decrease in the ohmic resistance for the cells with 0% SOC, e.g. in Fig. 3e, as their temperature increases are smaller as well. Nevertheless, it must be considered that the measured temperature on the cell surface is probably lower than the temperature within the cell and that significant temperature gradients within the cell are to be expected.

Regarding detection, this decrease of ohmic resistance for high frequencies in the case of soft ISC seems to offer no additional information to a temperature sensor, yet might confirm the benefit of sensorless temperature monitoring as presented in [42–47], when the use of temperature sensors is not feasible, as it could potentially warn users about an irregular temperature increase and thereby about the ISC and potential imminent hazardous events.

4.2.2. *Invalidity of measurements for lower frequencies*

To obtain a valid impedance measurement, the electrochemical system must approximately fulfill the criteria of linearity, stationarity and causality [54–56]. However for the chosen measurement option *fast* with a low repetition number some measurements (e.g. in Fig. 3d) do not show a smooth curve for low frequencies, but abrupt leaps of measurement points. As this indicates invalidity, Z-HIT (Zweipol-

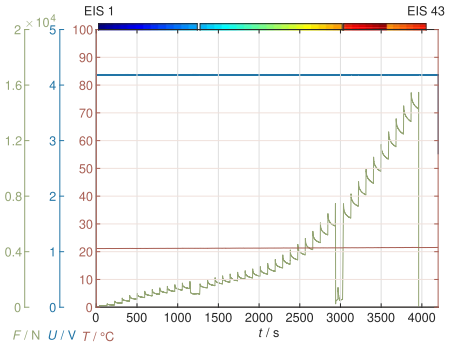

(a) F, U and T for cylindric impactor at 100 % SOC.

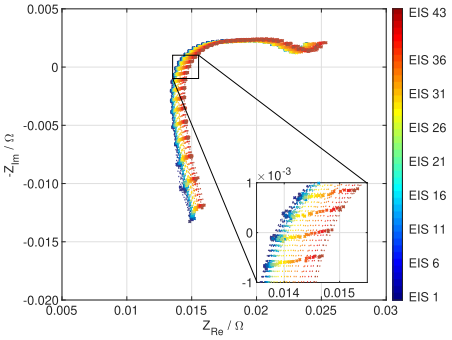

(b) Nyquist plot for cylindric impactor at 100 % SOC.

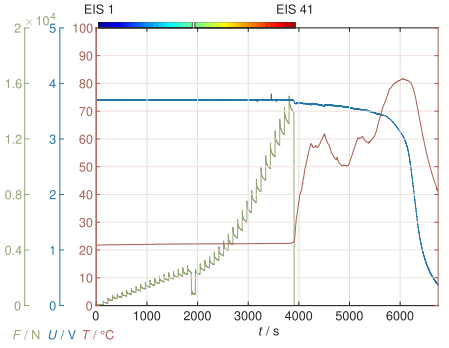

(c) F, U and T for cylindric impactor at 50 % SOC.

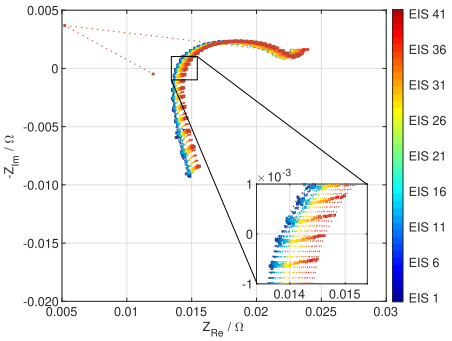

(d) Nyquist plot for cylindric impactor at 50 % SOC.

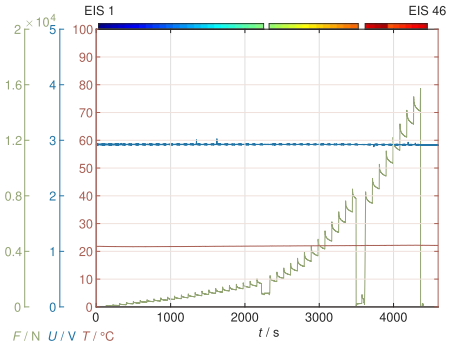

(e) F, U and T for cylindric impactor at 0 % SOC.

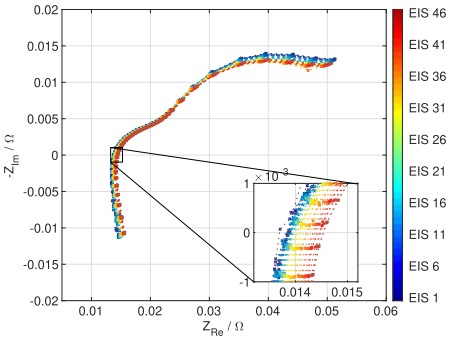

(f) Nyquist plot for cylindric impactor at 0 % SOC.

Fig. 4. Force, voltage, temperature (left column) and impedance measurements (right column) for abuse tests with cylindric impactor at various SOCs.

Hilbert-Transformation), which is a special form of Hilbert transformation for experimentally obtained impedance data [54,56], is exemplarily applied to the measurements 11 to 15 from the abuse tests with nail penetration and 50% SOC (Fig. 3d). Fig. 9a shows both the absolute values of $|Z|$ from the recorded measurement data set, as well as the data set that was reconstructed by the Z-HIT algorithm. Deviations between measured and reconstructed data indicate a violation of the required criteria to obtain valid measurements.

The Z-HIT confirms the valid measurements for EIS 11, while EIS 12, 13 and 14 become increasingly non-steady for frequencies below 100 Hz with the absolute resistance values decreasing, possibly due to temperature increase. The final EIS 15 shows a steady-state after the complete thermal runaway, which also supports the assumption of a direct connection between anode and cathode tabs.

In Fig. 9b, which depicts the Z-HIT for the nail penetration test with 0% SOC in Fig. 3e, likewise invalidity is shown for frequencies below 100 Hz, but with increasing absolute resistance values. Similar behavior was also observed in a test with a cell with 50% SOC, which was not further penetrated beyond the first occurrence of mild ISC after the voltage had dropped below 2.5 V.

As all invalid impedance spectra show temperature or voltage gradients during the measurements, and the charge exchange in the area of the ISC is likely irregular, the loss of validity is possibly linked to non-stationarity. The reason behind this is likely the longer measurement time per sine wave, resulting in larger changes within a single wave, while on the other hand fewer repetitions are performed for lower frequencies in the measurement setting *fast*, which prevents deviations from being evened out.

The analysis of the validity of the measurements for low frequencies might offer an approach for the detection of soft ISCs to alert users of an

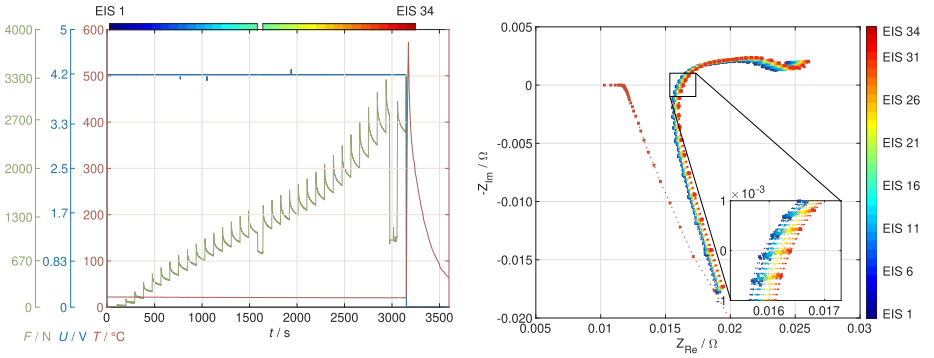

(a) F, U and T for hemispheric impactor at 100 % SOC.

(b) Nyquist plot for hemispheric impactor at 100 % SOC.

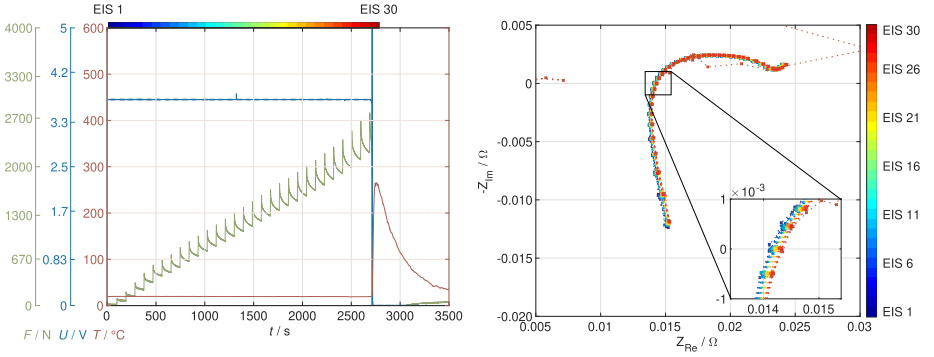

(c) F, U and T for hemispheric impactor at 50 % SOC.

(d) Nyquist plot for hemispheric impactor at 50 % SOC.

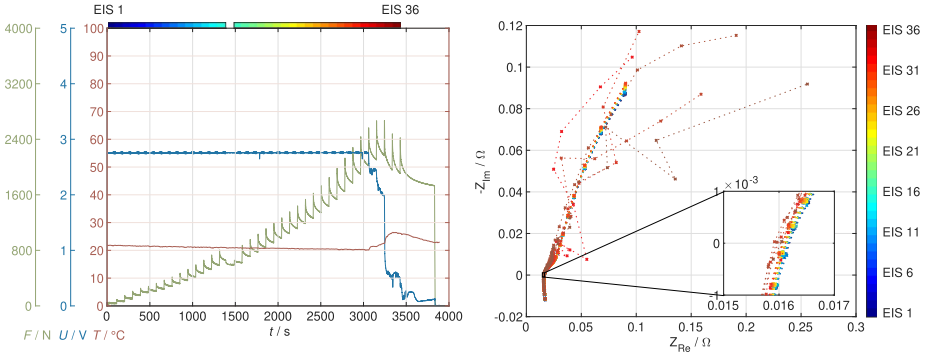

(e) F, U and T for hemispheric impactor at 0 % SOC.

(f) Nyquist plot for hemispheric impactor at 0 % SOC.

Fig. 5. Force, voltage, temperature (left column) and impedance measurements (right column) for abuse tests with hemispheric impactor at various SOCs.

upcoming hazardous event.

4.3. Impedance behavior due to compression

As observed for the cylindric impactor in Subsection 3.1.2 and on a smaller scale for the hemispheric impactor in Subsection 3.1.3, large area compression of 18,650 cells leads mainly to an increase in ohmic resistance and slight changes in impedance only for very high frequencies, as exemplarily depicted for the cylindric abuse test with 100% SOC in Fig. 10.

While post-mortem CT scans have shown different types of damaging mechanisms occurring during deformation, it is yet to discuss, which mechanisms are responsible for these changes:

- Compression of the separator and active material: Numerous publications link compression of jelly roll components to a decrease of porosity and a resulting increase of ion transport resistance in the active material and in the separator [57–60]. As a significant part of the jelly roll is affected by the compression in the cylindric and to a lesser extent in the hemispheric abuse tests, this mechanism offers a plausible explanation for the increase in ohmic resistance. This assumption is also supported by the observation that the increase of ohmic resistance is significantly larger for the large area deformation of the cell with the cylindric impactor than it is with the more local deformation of the hemispheric impactor.
- Delamination: Inhomogeneous compression and deformation of the cylindric jelly roll may lead to delamination and thereby to an increase of the effective charge transfer path and the reduction of total charge transfer surface area, which could, in turn, cause an increase of ohmic resistance. While the CT scans in Fig. 6 revealed only

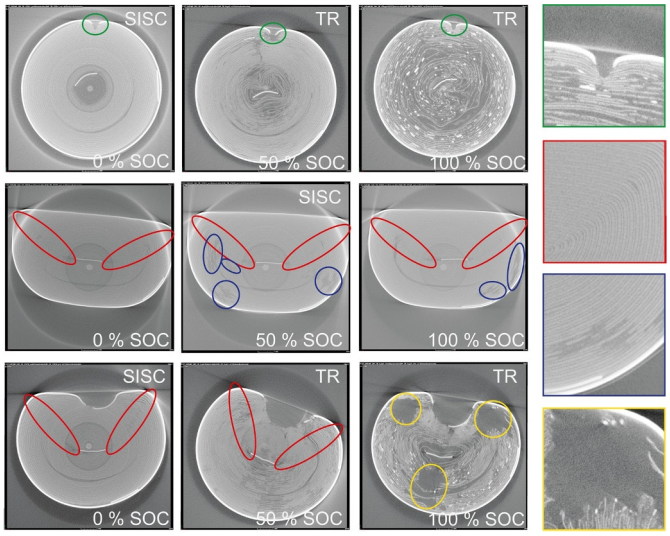

Fig. 6. Cross-sections of post-mortem CT scans. From left to right: 0% SOC, 50% SOC, 100% SOC and magnifications. From top to bottom: nail impactor, cylindric impactor, hemispheric impactor. Cells that showed soft ISC (SISC) or thermal runaway (TR) are labeled. Marked are nail penetration (green), buckling (red), cracking (blue) and material loss (yellow). (For interpretation of the references to color in this figure legend, the reader is referred to the web version of this article.)

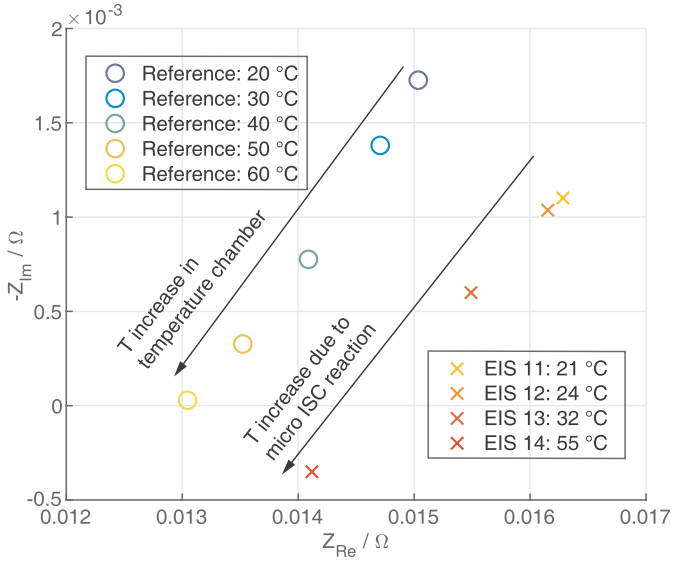

Fig. 8. Comparison of EIS at 400 Hz for nail penetration test with 50% SOC in Fig. 3d and reference measurements in a temperature chamber of a cell of the same type..

limited delamination in the buckling areas, the deformation may lead to the development of larger delamination areas and changes of the interfaces between the layers of the jelly roll, which are too small in distance for the resolution of the CT.

- Buckling of jelly roll layers: The buckling of the jelly roll layers can cause strong local compression of the separator and the active material. After severe buckling, the breaking and sharpening of the edges of the current collectors might lead to the perforation of the separator and thereby to electrical short circuit. However, the buckling radius is limited by the electrode thickness and strong buckling is generally not expected in the jelly roll at smaller deformations [29,61], which is also supported by investigations conducted by the authors. In contrast to this, a progressive resistance increase can already be observed at lower impactor forces. As the share of the electrode affected by this effect is also rather limited, as depicted in Fig. 6, the authors suspect that buckling only plays a minor role in the resistance increase.
- Cracks in electrode layer: As the cells with 50% and 100% SOC with cylindric impactor showed significant cracks in the electrode layers, while the 0% SOC cell with the cylindric impactor and the cells with the hemispheric impactor showed no cracks, yet all of them displayed resistance increases in the EIS, the authors consider it unlikely that cracking is the main reason for the observed EIS behavior. As cracking usually does not occur at very low strains [17,29,62], cracking as the decisive mechanism would also not match the progressive increase of ohmic resistance.
- Deformation of current collectors: The deflection of the current collector tabs could lead to the weakening of the welding spots connecting them to the poles due to tensile and shear forces, which in turn could cause an increase of ohmic resistance. The reshaping of the current collectors might also explain the stronger changes for very high frequencies in the tests with the cylindric impactor. Deformation tests with different angles towards the current collectors might give more insight into the influence of the current collector deformation.

While the compression of the separator and active material offers a plausible explanation for an increase of ohmic resistance, an open question remains why the test with the hemispherical impactor showed smaller increases for lower SOCs rather than higher SOCs. Potential mechanisms can be found in the change of the porous structure [58,59], the change of active material properties, which tend to get stiffer at higher SOCs [20,23,32,63], or the expansion characteristics of the active material due to the intercalation of lithium-ions [58,59,64–66]. This mechanism leads to up to 10% of volume expansion for fully lithiated graphite, which in turn results in larger void spaces within the cell and reduced initial stress levels in the jelly roll for uncharged cells. These void spaces could compensate a part of the deformation for lower SOCs. As the jolly roll undergoes significant compression at either SOC, another likely explanation could also be differences in electrochemical behavior of the materials under pressure [67].

The stronger changes in impedance for very high frequencies are possibly related to the change of the shape of the cell can and the

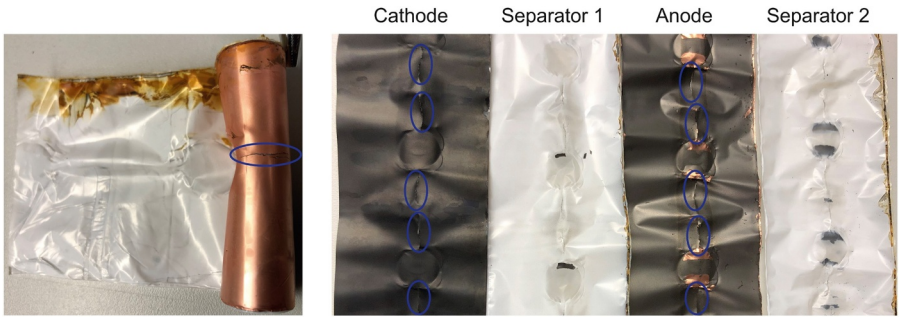

Fig. 7. Post mortem analysis for the abuse test with cylindric impactor at 100% SOC showing cracks (blue). Imprints of the buckling areas of the active material layers are also visible on the separators. The cell was deeply discharged before the disassembly. (For interpretation of the references to color in this figure legend, the reader is referred to the web version of this article.)

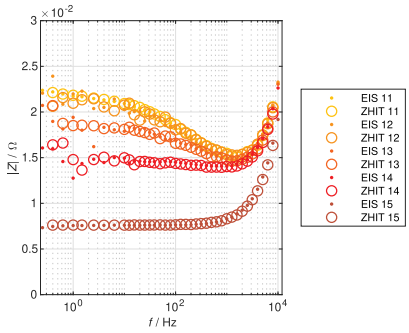

(a) Z-HIT for measurements 11 to 15 in Fig. 3d for nail penetration tests with 50 % SOC.

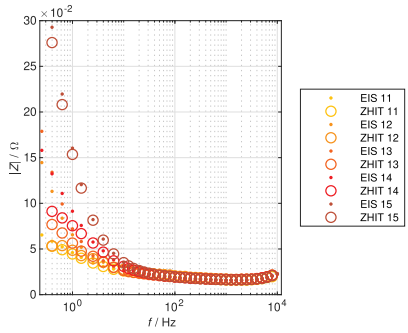

(b) Z-HIT for measurements 11 to 15 in Fig. 3e for nail penetration tests with 0 % SOC.

Fig. 9. Z-HIT for nail penetration tests with 0% and 50% SOC.

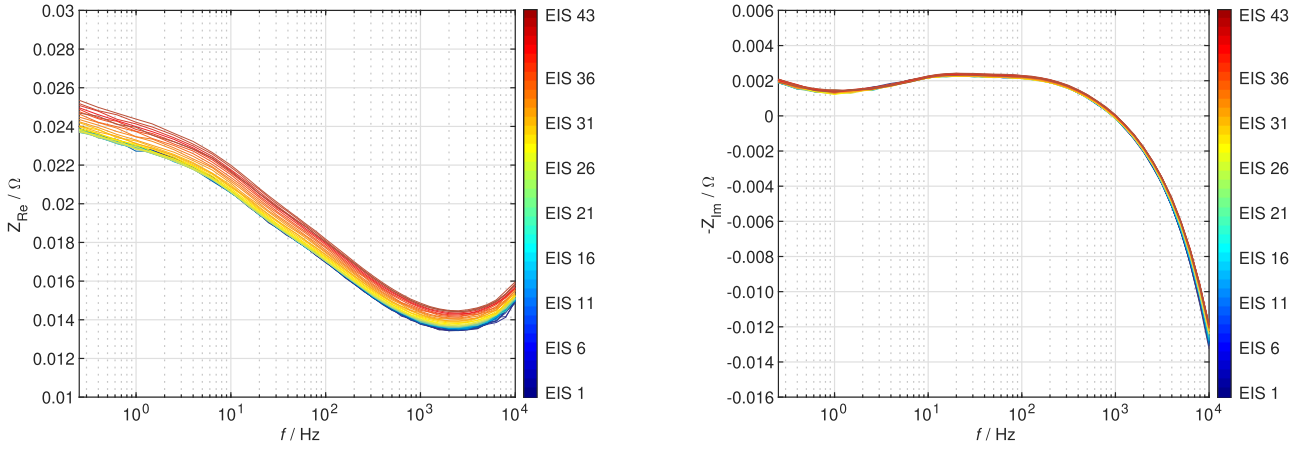

Fig. 10. Real and imaginary part for the test 4.1 with hemispheric impactor at 100% SOC as shown in Fig. 4b.

conductors within the jelly roll.

Regarding the detection of deforming events, the monitoring of ohmic resistance might offer an approach for the detection of mechanical deformation, but unlike load-displacement curves, which can exhibit drops of the force before the ISC [26], possibly due to buckling effects of the case, the EIS showed no pre-indicator of an upcoming ISC in the presented tests. Also, the stronger changes in impedance for very high frequencies might offer a method for damage detection.

5. Conclusion

In this work, a test series on 18,650 lithium-ion battery cells with various SOCs using different impactor geometries under stepwise loading with simultaneous impedance measurements is presented. The impedance measurements were analyzed and damage mechanisms were evaluated by CT. The analyzation revealed that local loading with a nail leads to no changes in EIS before the first occurrence of ISC, while large area compression leads to an increase of ohmic resistance with more significant changes for higher SOCs. Subsequently to soft ISCs, for high frequencies a decrease of ohmic resistance was observable, while measurements at low frequencies produced invalid impedance results.

After discussing possible mechanisms for these behaviors and potential approaches as detection methods for these behaviors, it is yet to analyze if the application of EIS is practicable in industry applications. The application of EIS as a detection method for mechanical induced deterioration is desirable, because voltage and current sensors are available in battery-monitoring-systems, even though the increased sample rates that are necessary for impedance measurements will require a certain technical effort. The necessary excitation can be superimposed on the operating currents and existing generators such as DC/DC-converters could be used for so-called passive impedance measurements. These measures would thus cause only moderate additional costs. Moreover, the method could be combined with other impedance-based monitoring technologies for state of power (SOP), SOH or temperature.

The experimental results of our work show that EIS offers a potential method for the detection of some damage scenarios while others, which were shown to avoid publication bias and to allow for neutral evaluation, remain undetected. This brings a restriction to EIS as a detection method as it is possibly suitable to detect specific unsafe states, but likely not sufficient to confirm a safe battery state. A certain increase of the real part of the impedance may be an indicator for a compression of the cell, as in the example of the cylindrical impactor, however the EIS shows no distinct pre-indicator of an upcoming ISC and a very small deformation on a large area can have the same implication on the EIS as a critical, but very local deformation. In all experiments, the relative change in impedance amounted to only a few percent, which will not be easy to measure outside laboratory conditions. For systems with a large number of parallel cells, the effective impedance change due to the mechanical deformation of a single cell would probably not be detectable. Another problem to be solved is the big number of parameters that also influence the EIS, such as SOC, SOH and temperature [40–46]. Therefore, a method solely relying on changes in the impedance seems inapt for the detection of upcoming mechanical damage. As deformation is expected to happen abruptly, an approach could be to monitor gradients rather than absolute values [49],

whereby a large gradient could indicate a critical event, or to combine impedance analysis with other indicators such as the detection of a critical acceleration of the battery pack. Besides the main goal to identify upcoming events in advance, impedance may also be an indicator that allows detecting temperature changes due to soft internal short circuits earlier than external temperature sensors.

With this said, the authors conclude that the application of EIS as a detection method for deforming mechanical damages will probably not be sufficient in industry applications if not supported with other methods. Nevertheless, impedance analysis provides valuable information and from a scientific point of view, several open questions are remaining, such as the behavior of different cell formats, chemistries and a fundamental understanding of the mechanism behind the dependency of the R_i under compression or the influence of the SOC.

Declaration of Competing Interest

The authors declare that they have no known competing financial interests or personal relationships that could have appeared to influence the work reported in this paper.

Acknowledgments

Funding from the German Federal Ministry for Economic Affairs and Energy (BMWi) of the project ReVISEDBatt [03ETE004C] and managing by the Projektträger Jülich (PtJ) is gratefully acknowledged. The authors also gratefully acknowledge TÜV SÜD Battery Testing GmbH, in particular, Michael Tillinger, Martin Knieling and Florian Amberger for kindly enabling the execution of the presented tests. The authors also want to thank Prof. Dr. Gregor Feiertag for supporting this project by granting access to the CT-scanner.

Appendix A. Test repetition

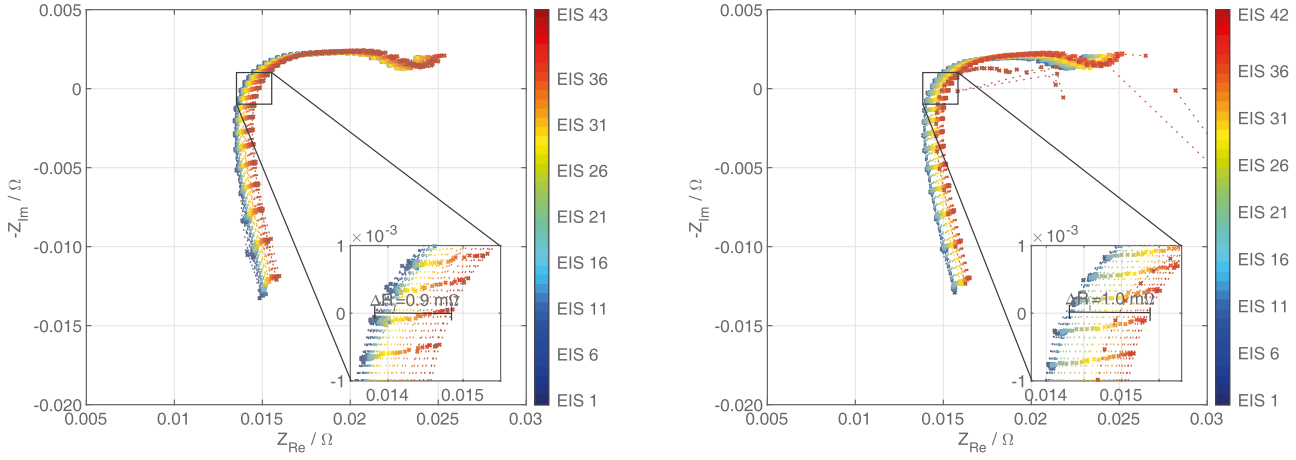

Fig. A.11. Comparision of the Nyquist plots for the tests (4.1 left, 4.2 right) with cylindric impactor at 100% SOC. (For interpretation of the references to color in text, the reader is referred to the web version of this article.)

References

[1] Q. Wang, P. Ping, X. Zhao, G. Chu, J. Sun, C. Chen, Thermal runaway caused fire and explosion of lithium ion battery, J. Power Sour. 208 (2012) 210–224, https://doi.org/10.1016/j.jpowsour.2012.02.038.

[2] S. Abada, G. Marlair, A. Lecocq, M. Petit, V. Sauvant-Moynot, F. Huet, Safety focused modeling of lithium-ion batteries: areview, J. Power Sour. 306 (2016) 178–192, https://doi.org/10.1016/j.jpowsour.2015.11.100.

[3] X. Feng, M. Ouyang, X. Liu, L. Lu, Y. Xia, X. He, Thermal runaway mechanism of lithium ion battery for electric vehicles: a review, Energy Storage Mater. 10 (2018) 246–267, https://doi.org/10.1016/j.ensm.2017.05.013.

[4] Y. Wang, J. Tian, Z. Chen, X. Liu, Model based insulation fault diagnosis for lithium-ion battery pack in electric vehicles, Measurement 131 (2019) 443–451, https://doi.org/10.1016/j.measurement.2018.09.007.

[5] B. Liu, Y. Jia, C. Yuan, L. Wang, X. Gao, S. Yin, J. Xu, Safety issues and mechanisms of lithium-ion battery cell upon mechanical abusive loading: a review, Energy Storage Mater. (2019), https://doi.org/10.1016/j.ensm.2019.06.036.

[6] R. Bubbico, V. Greco, C. Menale, Hazardous scenarios identification for Li-ion secondary batteries, Saf. Sci. 108 (2018) 72–88, https://doi.org/10.1016/j.ssci.2018.04.024.

[7] V. Ruiz, A. Pfrang, A. Kriston, N. Omar, P. van den Bossche, L. Boon-Brett, A review of international abuse testing standards and regulations for lithium ion batteries in electric and hybrid electric vehicles, Renew. Sustain. Energy Revi. 81 (2018) 1427–1452, https://doi.org/10.1016/j.rser.2017.05.195.

[8] J. Zhu, T. Wierzbicki, W. Li, A review of safety-focused mechanical modeling of commercial lithium-ion batteries, J. Power Sour. 378 (2018) 153–168, https://doi.org/10.1016/j.jpowsour.2017.12.034.

[9] J. Lamb, C.J. Orendorff, Evaluation of mechanical abuse techniques in lithium ion batteries, J. Power Sour. 247 (2014) 189–196, https://doi.org/10.1016/j.jpowsour.2013.08.066.

[10] B. Mao, H. Chen, Z. Cui, T. Wu, Q. Wang, Failure mechanism of the lithium ion battery during nail penetration, Int. J. Heat Mass Transf. 122 (2018) 1103–1115, https://doi.org/10.1016/j.ijheatmasstransfer.2018.02.036.

[11] J. Zhu, X. Zhang, E. Sahraei, T. Wierzbicki, Deformation and failure mechanisms of 18650 battery cells under axial compression, J. Power Sour. 336 (2016) 332–340, https://doi.org/10.1016/j.jpowsour.2016.10.064.

[12] I. Avdeev, M. Gilaki, Structural analysis and experimental characterization of cylindrical lithium-ion battery cells subject to lateral impact, J. Power Sour. 271 (2014) 382–391, https://doi.org/10.1016/j.jpowsour.2014.08.014.

[13] Z. Gao, X. Zhang, Y. Xiao, H. Gao, H. Wang, C. Piao, Influence of low-temperature charge on the mechanical integrity behavior of 18650 lithium-ion battery cells subject to lateral compression, Energies 12 (5) (2019) 797, https://doi.org/10.3390/en12050797.

[14] L. Greve, C. Fehrenbach, Mechanical testing and macro-mechanical finite element simulation of the deformation, fracture, and short circuit initiation of cylindrical Lithium ion battery cells, J. Power Sour. 214 (2012) 377–385, https://doi.org/10.1016/j.jpowsour.2012.04.055.

[15] M. Raffler, A. Sevarin, C. Ellersdorfer, S.F. Heindl, C. Breitfuss, W. Sinz, Finite element model approach of a cylindrical lithium ion battery cell with a focus on minimization of the computational effort and short circuit prediction, J. Power Sour. 360 (2017) 605–617, https://doi.org/10.1016/j.jpowsour.2017.06.028.

[16] E. Sahraei, J. Campbell, T. Wierzbicki, Modeling and short circuit detection of 18650 Li-ion cells under mechanical abuse conditions, J. Power Sour. 220 (2012) 360–372, https://doi.org/10.1016/j.jpowsour.2012.07.057.

[17] E. Sahraei, M. Kahn, J. Meier, T. Wierzbicki, Modelling of cracks developed in lithium-ion cells under mechanical loading, RSC Adv. 5 (98) (2015) 80369–80380, https://doi.org/10.1039/C5RA17865G.

[18] W. Wang, S. Yang, C. Lin, Clay-like mechanical properties for the jellyroll of cylindrical Lithium-ion cells, Appl. Energy 196 (2017) 249–258, https://doi.org/10.

1016/j.apenergy.2017.01.062.
[19] Q. Wang, B. Mao, S.I. Stoliarov, J. Sun, A review of lithium ion battery failure mechanisms and fire prevention strategies, Progr. Energy Combust. Sci. 73 (2019) 95–131, https://doi.org/10.1016/j.pecs.2019.03.002.
[20] J. Xu, B. Liu, D. Hu, State of charge dependent mechanical integrity behavior of 18650 lithium-ion batteries, Sci. Rep. 6 (2016) 21829, https://doi.org/10.1038/srep21829.
[21] M. Sheikh, A. Elmarakbi, M. Elkady, Thermal runaway detection of cylindrical 18650 lithium-ion battery under quasi-static loading conditions, J. Power Sour. 370 (2017) 61–70, https://doi.org/10.1016/j.jpowsour.2017.10.013.
[22] X. Feng, J. Sun, M. Ouyang, F. Wang, X. He, L. Lu, H. Peng, Characterization of penetration induced thermal runaway propagation process within a large format lithium ion battery module, J. Power Sour. 275 (2015) 261–273, https://doi.org/10.1016/j.jpowsour.2014.11.017.
[23] J. Xu, Y. Jia, B. Liu, H. Zhao, H. Yu, J. Li, S. Yin, Coupling effect of state-of-health and state-of-charge on the mechanical integrity of lithium-ion batteries, Exp. Mech. 58 (4) (2018) 633–643, https://doi.org/10.1007/s11340-018-0380-9.
[24] T. Kisters, E. Sahraei, T. Wierzbicki, Dynamic impact tests on lithium-ion cells, Int. J. Impact Eng. 108 (2017) 205–216, https://doi.org/10.1016/j.ijimpeng.2017.04.025.
[25] S.H. Chung, T. Tancogne-Dejean, J. Zhu, H. Luo, T. Wierzbicki, Failure in lithium-ion batteries under transverse indentation loading, J. Power Sour. 389 (2018) 148–159, https://doi.org/10.1016/j.jpowsour.2018.04.003.
[26] H. Luo, Y. Xia, Q. Zhou, Mechanical damage in a lithium-ion pouch cell under indentation loads, J. Power Sour. 357 (2017) 61–70, https://doi.org/10.1016/j.jpowsour.2017.04.101.
[27] W. Cai, H. Wang, H. Maleki, J. Howard, E. Lara-Curzio, Experimental simulation of internal short circuit in Li-ion and Li-ion-polymer cells, J. Power Sour. 196 (18) (2011) 7779–7783, https://doi.org/10.1016/j.jpowsour.2011.04.024.
[28] F. Ren, T. Cox, H. Wang, Thermal runaway risk evaluation of Li-ion cells using a pinch–torsion test, J. Power Sour. 249 (2014) 156–162, https://doi.org/10.1016/j.jpowsour.2013.10.058.
[29] H. Wang, S. Simunovic, H. Maleki, J.N. Howard, J.A. Hallmark, Internal configuration of prismatic lithium-ion cells at the onset of mechanically induced short circuit, J. Power Sour. 306 (2016) 424–430, https://doi.org/10.1016/j.jpowsour.2015.12.026.
[30] E. Sahraei, R. Hill, T. Wierzbicki, Calibration and finite element simulation of pouch lithium-ion batteries for mechanical integrity, J. Power Sour. 201 (2012) 307–321, https://doi.org/10.1016/j.jpowsour.2011.10.094.
[31] E. Sahraei, J. Meier, T. Wierzbicki, Characterizing and modeling mechanical properties and onset of short circuit for three types of lithium-ion pouch cells, J. Power Sour. 247 (2014) 503–516, https://doi.org/10.1016/j.jpowsour.2013.08.056.
[32] Y. Jia, S. Yin, B. Liu, H. Zhao, H. Yu, J. Li, J. Xu, Unlocking the coupling mechanical-electrochemical behavior of lithium-ion battery upon dynamic mechanical loading, Energy 166 (2019) 951–960, https://doi.org/10.1016/j.energy.2018.10.142.
[33] Y. Chen, S. Santhanagopalan, V. Babu, Y. Ding, Dynamic mechanical behavior of lithium-ion pouch cells subjected to high-velocity impact, Compos. Struct. 218 (2019) 50–59, https://doi.org/10.1016/j.compstruct.2019.03.046.
[34] B. Liu, Y. Jia, J. Li, S. Yin, C. Yuan, Z. Hu, L. Wang, Y. Li, J. Xu, Safety issues caused by internal short circuits in lithium-ion batteries, J. Mater. Chem. A 6 (43) (2018) 21475–21484, https://doi.org/10.1039/C8TA08997C.
[35] T. Ma, L. Chen, S. Liu, Z. Zhang, S. Xiao, B. Fan, L. Liu, C. Lin, S. Ren, F. Wang, Mechanics-morphologic coupling studies of commercialized lithium-ion batteries under nail penetration test, J. Power Sour. 437 (2019) 226928, https://doi.org/10.1016/j.jpowsour.2019.226928.
[36] A. Simeone, D. Lv, X. Liu, J. Zhang, Collision damage assessment in lithium-ion battery cells via sensor monitoring and ensemble learning, Procedia CIRP (2018) 273–278, https://doi.org/10.1016/j.procir.2018.09.073.
[37] C. Pastor-Fernández, K. Uddin, G.H. Chouchelamane, W.D. Widanage, J. Marco, A comparison between electrochemical impedance spectroscopy and incremental capacity-differential voltage as Li-ion diagnostic techniques to identify and quantify the effects of degradation modes within battery management systems, J. Power Sour. 360 (2017) 301–318, https://doi.org/10.1016/j.jpowsour.2017.03.042.
[38] C. Pastor-Fernández, T.F. Yu, W.D. Widanage, J. Marco, Critical review of non-invasive diagnosis techniques for quantification of degradation modes in lithium-ion batteries, Renew. Sustain. Energy Revi. 109 (2019) 138–159, https://doi.org/10.1016/j.rser.2019.03.060.
[39] A. Barai, K. Uddin, M. Dubarry, L. Somerville, A. McGordon, P. Jennings, I. Bloom, A comparison of methodologies for the non-invasive characterisation of commercial Li-ion cells, Progr. Energy Combust. Sci. 72 (2019) 1–31, https://doi.org/10.1016/j.pecs.2019.01.001.
[40] C.T. Love, M.B. Virji, R.E. Rocheleau, K.E. Swider-Lyons, State-of-health monitoring of 18650 4S packs with a single-point impedance diagnostic, J. Power Sour. 266 (2014) 512–519, https://doi.org/10.1016/j.jpowsour.2014.05.033.
[41] C. Love, M. Dubarry, T. Reshetenko, A. Devie, N. Spinner, K. Swider-Lyons, R. Rocheleau, Lithium-ion cell fault detection by single-point impedance diagnostic and degradation mechanism validation for series-wired batteries cycled at 0 Â °C, Energies 11 (4) (2018) 834, https://doi.org/10.3390/en11040834.
[42] J.P. Schmidt, S. Arnold, A. Loges, D. Werner, T. Wetzel, E. Ivers-Tiffée, Measurement of the internal cell temperature via impedance: evaluation and application of a new method, J. Power Sour. 243 (2013) 110–117, https://doi.org/10.1016/j.jpowsour.2013.06.013.
[43] R.R. Richardson, P.T. Ireland, D.A. Howey, Battery internal temperature estimation by combined impedance and surface temperature measurement, J. Power Sour. 265 (2014) 254–261, https://doi.org/10.1016/j.jpowsour.2014.04.129.
[44] H. Beelen, L. Raijmakers, M. Donkers, P. Notten, H.J. Bergveld, A comparison and accuracy analysis of impedance-based temperature estimation methods for Li-ion batteries, Appl. Energy 175 (2016) 128–140, https://doi.org/10.1016/j.apenergy.2016.04.103.
[45] L. Raijmakers, D.L. Danilov, J. van Lammeren, M. Lammers, P. Notten, Sensorless battery temperature measurements based on electrochemical impedance spectroscopy, J. Power Sour. 247 (2014) 539–544, https://doi.org/10.1016/j.jpowsour.2013.09.005.
[46] N.S. Spinner, C.T. Love, S.L. Rose-Pehrsson, S.G. Tuttle, Expanding the operational limits of the single-point impedance diagnostic for internal temperature monitoring of lithium-ion batteries, Electrochim. Acta 174 (2015) 488–493, https://doi.org/10.1016/j.electacta.2015.06.003.
[47] R. Srinivasan, P.A. Demirev, B.G. Carkhuff, Rapid monitoring of impedance phase shifts in lithium-ion batteries for hazard prevention, J. Power Sour. 405 (2018) 30–36, https://doi.org/10.1016/j.jpowsour.2018.10.014.
[48] J. Seifert, J.P. Schmidt, A novel impedance-based method for structural monitoring of automotive lithium-ion battery packs, Conference: The 12th International Workshop on Structural Health Monitoring, (2019).
[49] E. Cabrera-Castillo, F. Niedermeier, A. Jossen, Calculation of the state of safety (SOS) for lithium ion batteries, J. Power Sour. 324 (2016) 509–520, https://doi.org/10.1016/j.jpowsour.2016.05.068.
[50] F.M. Kindermann, A. Noel, S.V. Erhard, A. Jossen, Long-term equalization effects in Li-ion batteries due to local state of charge inhomogeneities and their impact on impedance measurements, Electrochim. Acta 185 (2015) 107–116, https://doi.org/10.1016/j.electacta.2015.10.108.
[51] Y. Shi, D.J. Noelle, M. Wang, A.V. Le, H. Yoon, M. Zhang, Y.S. Meng, Y. Qiao, Exothermic behaviors of mechanically abused lithium-ion batteries with dibenzylamine, J. Power Sour. 326 (2016) 514–521, https://doi.org/10.1016/j.jpowsour.2016.07.034.
[52] B.M. Huhman, J.M. Heinzel, L. Mili, C.T. Love, D.A. Wetze, Investigation into state-of-health impedance diagnostic for 266504P1S battery packs, J. Electrochem. Soc. (2017).
[53] D.P. Finegan, M. Scheel, J.B. Robinson, B. Tjaden, I. Hunt, T.J. Mason, J. Millichamp, M. Di Michiel, G.J. Offer, G. Hinds, D.J.L. Brett, P.R. Shearing, In-operando high-speed tomography of lithium-ion batteries during thermal runaway, Nat. Commun. 6 (2015) 6924, https://doi.org/10.1038/ncomms7924.
[54] H. Zappen, F. Ringbeck, D. Sauer, Application of time-resolved multi-sine impedance spectroscopy for lithium-ion battery characterization, Batteries 4 (4) (2018) 64, https://doi.org/10.3390/batteries4040064.
[55] Urquidi-Macdonald, S. Real, D.D. .Macdonald, Applications of Kramers—Kronig transforms in the analysis of electrochemical impedance data—III. Stability and linearity, Electrochim. Acta (1990).
[56] C.A. Schiller, F. Richter, E. Gülzow, N. Wagner, Validation and evaluation of electrochemical impedance spectra of systems with states that change with time, Phys. Chem. Chem. Phys. 3 (3) (2001) 374–378, https://doi.org/10.1039/b007678n.
[57] J. Cannarella, C.B. Arnold, Ion transport restriction in mechanically strained separator membranes, J. Power Sour. 226 (2013) 149–155, https://doi.org/10.1016/j.jpowsour.2012.10.093.
[58] D. Sauerteig, Implementierung und Parametrierung eines physikalischen Simulationsmodells einer Lithium-Ionen Zelle zur Analyse elektrochemisch-mechanischer Wechselwirkungen (2018).
[59] D. Sauerteig, N. Hanselmann, A. Arzberger, H. Reinshagen, S. Ivanov, A. Bund, Electrochemical-mechanical coupled modeling and parameterization of swelling and ionic transport in lithium-ion batteries, J. Power Sour. 378 (2018) 235–247, https://doi.org/10.1016/j.jpowsour.2017.12.044.
[60] A. Barai, R. Tangirala, K. Uddin, J. Chevalier, Y. Guo, A. McGordon, P. Jennings, The effect of external compressive loads on the cycle lifetime of lithium-ion pouch cells, J. Energy Storage 13 (2017) 211–219, https://doi.org/10.1016/j.est.2017.07.021.
[61] M.Y. Ali, W.-J. Lai, J. Pan, Computational models for simulations of lithium-ion battery cells under constrained compression tests, J. Power Sour. 242 (2013) 325–340, https://doi.org/10.1016/j.jpowsour.2013.05.022.
[62] J. Lian, T. Wierzbicki, J. Zhu, W. Li, Prediction of shear crack formation of Lithium-ion batteries under rod indentation: comparison of seven failure criteria, Eng. Fract. Mech. (2019) 106520, https://doi.org/10.1016/j.engfracmech.2019.106520.
[63] L. Wang, S. Yin, C. Zhang, Y. Huan, J. Xu, Mechanical characterization and modeling for anodes and cathodes in lithium-ion batteries, J. Power Sour. 392 (2018) 265–273, https://doi.org/10.1016/j.jpowsour.2018.05.007.
[64] J. Park, S. Kalnaus, S. Han, Y.K. Lee, G.B. Less, N.J. Dudney, C. Daniel, A.M. Sastry, In situ atomic force microscopy studies on lithium (de)intercalation-induced morphology changes in LixCoO2 micro-machined thin film electrodes, J. Power Sour. 222 (2013) 417–425, https://doi.org/10.1016/j.jpowsour.2012.09.017.
[65] B. Rieger, S. Schlueter, S.V. Erhard, J. Schmalz, G. Reinhart, A. Jossen, Multi-scale investigation of thickness changes in a commercial pouch type lithium-ion battery, J. Energy Storage 6 (2016) 213–221, https://doi.org/10.1016/j.est.2016.01.006.
[66] J.H. Lee, H.M. Lee, S. Ahn, Battery dimensional changes occurring during charge/discharge cycles—thin rectangular lithium ion and polymer cells, J. Power Sour. 119–121 (2003) 833–837, https://doi.org/10.1016/S0378-7753(03)00281-7.
[67] Y. Zhao, P. Stein, Y. Bai, M. Al-Siraj, Y. Yang, B.-X. Xu, A review on modeling of electro-chemo-mechanics in lithium-ion batteries, J. Power Sour. 413 (2019) 259–283, https://doi.org/10.1016/j.jpowsour.2018.12.011.